



The Thermodynamics of Rotating Black Hole Star Clusters

Andrei Gruzinov¹, Yuri Levin^{2,3,4}, and Jiarong Zhu¹

¹CCPP, Department of Physics, New York University, New York, NY 10001, USA

²Physics Department and Columbia Astrophysics Laboratory, Columbia University, 538 West 120th Street, New York, NY 10027, USA

³Center for Computational Astrophysics, Flatiron Institute, 162 5th Avenue, NY 10011, USA

⁴School of Physics and Astronomy, Monash University, Clayton VIC 3800, Australia

Received 2020 July 15; revised 2020 September 30; accepted 2020 October 7; published 2020 December 7

Abstract

Rotating star clusters near supermassive black holes are studied using Touma–Tremaine thermodynamics of gravitationally interacting orbital ellipses. A simple numerical procedure for calculating thermodynamic equilibrium states for an arbitrary distribution of stars over masses and semimajor axes is described. Spontaneous symmetry breaking and breakdown of thermodynamics at low positive temperatures are rigorously proven for nonrotating clusters. Rotation is introduced through a second temperature-like parameter. Both axially symmetric and lopsided rotational equilibria are found; the lopsided equilibria precess with the angular velocity that is given by the ratio of the two temperatures. The eccentric stellar disk in the nucleus of the Andromeda galaxy may be an example of a lopsided thermodynamic equilibrium of a rotating black hole star cluster. Stellar-mass black holes occupy highly eccentric orbits in broken-symmetry star clusters, and form flattened disklike configurations in rotating star clusters. They are attracted to orbits that are stationary in the frame of reference rotating with the angular velocity of the cluster. In spherical clusters, stellar-mass black holes' orbits are significantly more eccentric than those of the lighter stars if the temperature is negative and more circular if the temperature is positive. Finally, we note that planets, comets, dark matter particles, and other light bodies tend to form a spherically symmetric nonrotating subcluster with maximum-entropy eccentricity distribution $s_{\text{cr}}P(e) = 2e$, even if their host cluster is rotating and lopsided.

Unified Astronomy Thesaurus concepts: [Supermassive black holes \(1663\)](#); [Astrophysical black holes \(98\)](#); [Stellar dynamics \(1596\)](#)

1. Introduction

An old subject of orbital dynamics in near-Keplerian potentials has been revived over the past two decades, in order to achieve a deeper understanding of the dynamics of stellar-mass objects near supermassive black holes in galactic nuclei. Since the work of Rauch & Tremaine (1996), it has been understood that secular, orbit-averaged interactions between the stellar orbits play a dominant role in determining the evolution of angular momenta and eccentricities of the orbits. The relatively fast secular dynamics leaves the semimajor axes of the orbits unchanged; the axes evolve on a much longer timescale due to two-body gravitational scattering of the stars. It is thus of considerable interest to explore a purely secular evolution of black hole star clusters.

The original insight has since been complemented by a large set of numerical and analytical explorations of the secular dynamics (Gürkan & Hopman 2007; Madigan et al. 2011; Merritt et al. 2011; Hamers et al. 2014; Bar-Or & Alexander 2016; Sridhar & Touma 2016a, 2016b; Bar-Or & Fouvy 2018; Fouvy & Bar-Or 2018). The purpose of these works was to find an effective description of the stochastic evolution of the orbital parameters of individual stars, dubbed “resonant relaxation” by Rauch & Tremaine (1996).

The outcome of resonant relaxation was studied in a series of papers: Touma & Tremaine (2014), Touma et al. (2019), Tremaine (2020a), and Tremaine (2020b); hereafter, these four papers are referred to as TT. TT argued that secular dynamics allows equilibria states that can be described by a language of conventional statistical mechanics, with temperature T serving as a measure of the self-gravitation energy of the cluster. That such equilibria exist at all is a highly nontrivial result. In general, a stellar cluster never reaches thermodynamic equilibrium but rather

keeps evaporating and forming tight binaries. But in a black hole star cluster, as explained by TT, the pointlike stars (which indeed never reach thermodynamic equilibrium) can be replaced by Keplerian ellipses, and the latter do equilibrate. One can show that the timescale for achieving this equilibrium is much shorter than the lifetime of the clusters.⁵ Therefore, the secular-dynamical equilibrium of Keplerian ellipses corresponds to an intermediate-asymptotic state of a real cluster, with the relaxed distribution of stellar eccentricities and inclinations but continuing evolution of the orbital energies.

It is convenient to define $\beta = 1/T$; TT showed that β can be both positive and negative. Remarkably, while nonrotating low- β equilibria are spherically symmetric, the high- β (low positive temperature) equilibria turned out to be nonspherical and lopsided. Interestingly, somewhat earlier, Roupas et al. (2017) studied the case where the eccentricities of the stars were fixed but the orbital planes were allowed to change (the case of so-called vector resonant relaxation), and they also found phase transitions that led to nonspherical, albeit nonlopsided equilibria. The TT phase transition and associated lopsided gravitational potentials and stellar configurations have important practical implications for the stellar and gas dynamics near supermassive black holes. However, TT demonstrated this behavior only for special cases (one article for each case) and did not give a general proof for the existence of the phase transition.

⁵ It is important to emphasize that what we are considering is a collisional equilibrium, in that it is achieved through pairwise gravitational interaction of orbital ellipses. In the limit where the number of stars tends to infinity while keeping the total mass fixed, a different collisionless equilibrium is reached; for general discussions of such equilibria in systems with long-range forces, see, e.g., Levin et al. (2008).

This paper advances TT's discovery in several ways. First, we devise a simple numerical algorithm that allows us to compute the thermal equilibria of stellar clusters with any distribution of semimajor axes and stellar masses.

Second, we give a general proof for the existence of the phase transition and elucidate the limits of applicability for thermodynamical treatment, pointing out that the full partition function diverges for sufficiently high β (low positive temperatures).

Third, we add rotation to the cluster (this was done in Touma & Tremaine 2014 for disks but not for three-dimensional clusters) and numerically explore both low- β axially symmetric equilibria and high- β lopsided equilibria that precess with a fixed angular velocity. We demonstrate the latter configurations that appear similar to the eccentric nuclear stellar disk in Andromeda (Tremaine 1995).

Fourth, we explore the equilibrium configurations of stellar-mass black holes that are much heavier than average members of the cluster. We find, e.g., that they cluster on strongly eccentric orbits in lopsided nonrotating equilibria and form strongly flattened disklike structures in rotating clusters.

Ideally, the results of this paper should be confirmed by direct numerical simulations of N -body systems with a supermassive black hole as one of the bodies. However, the very feature that allows our analytical treatment, i.e., the slow evolution of the Keplerian ellipses, makes it extremely computationally expensive to extract the features of secular dynamics from direct simulations. Thus, the lopsided equilibria have so far only been confirmed by simulations with interacting Keplerian ellipses, not by direct simulations of stellar motion.

The plan of the paper is as follows. In Section 2, we describe the general formalism for thermodynamic equilibria of black hole clusters. In Section 3, we give a proof for spontaneous symmetry breaking in nonrotating clusters and describe the limits of applicability of thermodynamics. In Section 4, we describe the numerical algorithm for constructing equilibria, and in Section 5, we present the results of our numerical experiments. In Section 6, we analytically explore the distributions of stellar-mass black holes in both spherical and rotating clusters. We also comment on the universality of the distribution of light objects. We conclude in Section 7 by briefly discussing the possible astrophysical implications of our findings.

2. Nonlinear Poisson Equation

The secular-dynamical equilibrium state of a black hole star cluster is achieved by evolution of the stellar Keplerian ellipses, in which the semimajor axes remain unchanged, while all other orbital parameters relax, preserving only the integrals of motion. Therefore, at least one thermodynamic equilibrium state must exist for any set of quantities (F, U, \mathbf{J}) , where

1. $F(A)$ is the distribution function of stars over masses m and semimajor axes a . We define a composite $A \equiv (m, a)$, with the number of stars $N = \int dA F(A)$, $dA \equiv dm da$; and
2. U is the potential energy of gravitationally attracting ellipses. The mass of each star is spread over its ellipse in proportion to the orbital time, as spelled out below; and
3. \mathbf{J} is the total angular momentum of the stars.

For a given set (F, U, \mathbf{J}) , in the mean-field approximation, the thermodynamic equilibrium state is characterized by

1. $\phi(\mathbf{r})$, the equilibrium gravitational potential of the stars only (the Keplerian potential of the black hole not included); and
2. $f(A, B)$, the equilibrium distribution function of stars over masses m and semimajor axes a , eccentricities e , and ellipse orientations, given by unit vectors along the major and minor axes \hat{n}_1, \hat{n}_2 . Here we have introduced another composite variable, $B \equiv (e, \hat{n}_1, \hat{n}_2)$. The total number of stars is given by

$$N = \int dA dB f(A, B), \quad (1)$$

where

$$dB \equiv de^2 d^2n_1 d^2n_2 \delta(\hat{n}_1 \cdot \hat{n}_2) \quad (2)$$

and $d^2n_{1,2}$ are the differential solid angles.

In statistical physics language, the cluster can be represented by a microcanonical ensemble with two additive conserved quantities: energy and angular momentum. Therefore, in the mean-field theory approximation, the canonical equilibrium distribution function has Boltzmann-like factors for both energy and angular momentum (see also Touma & Tremaine 2014 for derivation using the maximum-entropy argument). It is given by

$$f(A, B) = \frac{F(A)}{Z(A)} \exp[-\beta u(A, B) + \vec{\gamma} \cdot \mathbf{j}(A, B)], \quad (3)$$

as follows.

1. Here $u(A, B), \mathbf{j}(A, B)$ are the gravitational potential energy due to the gravitational field from other ellipses and the angular momentum of the (A, B) ellipse. They are given by

$$\mathbf{j}(A, B) = [GMm^2a(1 - e^2)]^{1/2} \hat{n}_1 \times \hat{n}_2, \quad (4)$$

where M is the black hole mass, and

$$\begin{aligned} u(A, B) &= m \langle \phi \rangle = \frac{m}{P} \int_0^{2\pi} d\xi \frac{dt}{d\xi} \phi(\mathbf{R}) \\ &= \frac{m}{2\pi a} \int_0^{2\pi} d\xi R \phi(\mathbf{R}). \end{aligned} \quad (5)$$

Here ξ is the eccentric anomaly of a point on the Keplerian ellipse, $\mathbf{R}(\xi)$ and $t(\xi)$ are the corresponding position and time from the periastron passage, and P is the orbital period. These quantities are given by

$$P(A) = 2\pi (GM)^{-1/2} a^3/2, \quad (6)$$

$$t(\xi; A, B) = \frac{P(A)}{2\pi} (\xi - e \sin \xi), \quad (7)$$

$$\mathbf{R}(\xi; A, B) = a(\cos \xi - e)\hat{n}_1 + a\sqrt{1 - e^2} \sin \xi \hat{n}_2. \quad (8)$$

2. As defined in the Introduction, β is the inverse temperature. It can be either positive or negative, since the phase space of Keplerian ellipses with fixed semimajor axis is compact.⁶
3. Here γ is a three-dimensional vector of inverse temperature-like quantities corresponding to the components of angular momentum \mathbf{J} . For nonzero β , the factor in the

⁶ The possibility of the temperature being negative for systems with compact phase spaces was first pointed out by Onsager (1949).

exponential can be rewritten as $-\beta u_j$, where

$$\begin{aligned} u_j &\equiv u - \boldsymbol{\Omega} \cdot \mathbf{j} \\ \boldsymbol{\Omega} &\equiv \vec{\gamma}/\beta. \end{aligned} \quad (9)$$

The quantity u_j has the form of the Jacobi integral, a conserved quantity in a potential that is rotating with angular velocity $\boldsymbol{\Omega}$. By Jean’s theorem, the steady-state distributions in such a rotating frame should be a function only of u_j . Therefore, if the solution we find is nonaxisymmetric with respect to $\vec{\gamma}$, it should be interpreted as a solution that is obtained in a frame that is rotating with the angular velocity $\boldsymbol{\Omega}$ (we thank Scott Tremaine for clarifying this point). As we show below, a precessing eccentric nuclear disk in Andromeda is a possible example of such a solution. Conversely, for sufficiently “hot” systems with large $\boldsymbol{\Omega}$, no nonaxisymmetric solutions can exist; it would be unphysical for a lopsided system to precess with large angular velocity.

In actual numerical calculations, we use $\cosh[\gamma \cdot \mathbf{j}]$ rather than $\exp[\gamma \cdot \mathbf{j}]$ for the angular momentum Boltzmann factor because any ellipse can be traced in two opposite directions. This allows us to use nonoriented ellipses and save on the configuration space sampling.

4. Here $Z(A)$ is the statistical sum, which must be calculated for each set of parameters A separately, because $A = \text{const}$ during the secular-dynamical relaxation of the cluster:

$$Z(A) = \int dB e^{-\beta u(A,B)} \cosh[\vec{\gamma} \cdot \mathbf{j}(A, B)]. \quad (10)$$

The gravitational potential of the ellipses is given by the nonlinear Poisson equation

$$\nabla^2 \phi = 4\pi G \rho, \quad (11)$$

where the density ρ is given by

$$\begin{aligned} \rho(\mathbf{r}) &= \int dA dB f(A, B) \frac{m}{P(A)} \\ &\times \int_0^{2\pi} d\xi \frac{dt(\xi; A, B)}{d\xi} \delta[\mathbf{r} - \mathbf{R}(\xi; A, B)]. \end{aligned} \quad (12)$$

The Poisson equation is nonlinear because the distribution function $f(A, B)$ nonlinearly depends on the gravitational potential ϕ .

3. Proof of Spontaneous Symmetry Breaking. The Minimal Temperature Phenomenon

There are two remarkable features of the black hole star cluster thermodynamics: (1) the spontaneous symmetry breaking at low temperatures, which has been demonstrated for particular configurations in TT, and (2) the existence of positive “minimum temperature” T_c , which is described here for the first time. For values $\beta > 1/T_c$, the full statistical sum diverges and the function $f(A, B)$ collapses to a singular distribution. We note that such singular distributions have infinite binding energy. We emphasize that the divergence of the full statistical sum does not imply that no microcanonical ensemble with finite energy and mean-field Boltzmann distributions with $\beta > 1/T_c$ can exist. It does imply that if

the cluster interacts with the heat bath with $\beta > 1/T_c$, it will collapse to a degenerate state.

The existence of the symmetry breaking and minimum temperature is described analytically and rigorously proven in this section. The qualitative understanding of black hole star clusters gives us confidence that our numerical results should be correct, as we do see both the symmetry breaking and the low-temperature singularity in Section 5. Our analytical proof is much simpler and more universal than the arguments in TT.

We are able to prove the spontaneous symmetry breaking in nonrotating clusters only with $\gamma = 0$ in Equation (3); in other words, we are able to prove the breaking of spherical symmetry. Axial symmetry breaking occurs in rotating clusters too because (1) by continuity, we expect it to take place at small γ and (2) we observe it in numerical simulations. Still, our proof works only for the nonrotating clusters.

The minimal temperature phenomenon, i.e., the breakdown of Touma–Tremaine thermodynamics at sufficiently low temperatures, is valid and proved below for clusters with arbitrary rotation. This proof is an immediate extension of lemma (1) of the symmetry breaking proof.

The spherical symmetry breaking follows from two observations.

Lemma (1). For any given distribution $F(A)$ assumed “nice” enough, there exist initial (thermodynamically unrelaxed) distributions $f(A, B)$ with arbitrarily large binding energy $|U|$.

Lemma (2). For any given distribution $F(A)$, all spherically symmetrical states have binding energy below a certain maximal value. It follows that the only way to cool down the cluster, that is, to increase the binding energy, is to break the spherical symmetry. We now prove lemmas (1) and (2) in turn.

To prove lemma (1), assume that all orbital ellipses are degenerate, with $e = 1$, and aligned along a single direction x . Then, $U = -\infty$, because

$$\int \frac{dx_1 dx_2 \chi(x_1) \chi(x_2)}{|x_1 - x_2|} = \infty. \quad (13)$$

Here $\chi(x)$ is the linear density along x .

The divergence is logarithmic in x and therefore also logarithmic in the eccentricity deviation from unity and the misalignment angle of different ellipses. This leads to the interesting minimal temperature phenomenon: Touma–Tremaine thermodynamics breaks down at small positive temperatures, because the full statistical sum $Z = \int dA F(A) Z(A)$ diverges algebraically for $\beta > \beta_c > 0$. To prove the statement and get an estimate of the critical temperature $T_c \equiv \beta_c^{-1}$, consider nearly degenerate ellipses, $e = 1 - \epsilon$, $\epsilon \ll 1$, which are nearly aligned; that is, the ellipses have major-axis directions within a cone of opening angle $\theta \ll 1$. For convenience, we assume that the ellipses have similar semimajor axes $\sim a$ (this assumption is easy to relax but facilitates exposition of the main point). Since the minor axes of the ellipses are $\sim \epsilon^{1/2} a$, all of the mass of the stars lies within a cylinder of length $\sim a$ and radius $\sim \max(\epsilon^{1/2}, \theta) a$. Then, the self-gravitational energy of N stars of mass $\sim m$ is, to logarithmic accuracy,

$$U \sim \frac{GN^2 m^2}{a} \ln \max(\epsilon^{1/2}, \theta). \quad (14)$$

The phase-space volume of our nearly aligned and almost degenerate ellipses is $V_{\text{ph}} \propto (\epsilon \theta^2)^N$. The contribution of these

ellipses to the statistical sum (exact, not the mean-field) scales as

$$\propto V_{\text{ph}} e^{-\beta U} \quad (15)$$

and diverges for small ϵ , θ if and only if $\beta > \beta_c$,

$$\beta_c^{-1} \equiv T_c \sim \frac{GNm^2}{a}. \quad (16)$$

When the positive temperature is lowered below T_c , the full distribution function should collapse to degenerate ellipses.⁷ Note that T_c corresponds to the typical binding energy of a star to the cluster and is thus comparable to a natural temperature scale of the cluster. The collapse is readily observed in our numerical simulations, as described in Section 5. We note that physically, the collapse to a degenerate state can take place if the cluster interacts with the heat bath that is able to absorb a formally infinite amount of the degenerate state's binding energy.

Lemma (2) is most easily proved by recalling that in a spherical black hole star cluster, an elliptical orbit precesses in a direction that is retrograde with respect to its orbital motion.⁸ This statement is proved in Section 3.2 of Tremaine (2005). The angular frequency of the precession equals $\partial u / \partial j$, and “retrograde” implies that this is < 0 . Here u is the orbit-averaged potential energy of the star, j is the magnitude of its angular momentum, and the derivative is evaluated while keeping the orbital semimajor axis fixed. It follows that the energy of the orbit is reduced as the orbit becomes more circular. Applying this to all orbits at the same time, we see that for a given $F(A) = F(a, m)$, the gravitational energy U of the cluster is minimized (and its binding energy is maximized) if all orbits are circular. This minimal energy is given by

$$U_{\min} = - \int da \frac{GM_{\text{cluster}}(<a)}{a} \int dm m F(a, m), \quad (17)$$

where $M_{\text{cluster}}(<a)$ is the stellar mass inside radius a ,

$$M_{\text{cluster}}(<a) = \int_0^a da_1 \int dm_1 m_1 F(a_1, m_1). \quad (18)$$

As we saw from lemma (1), there are cluster configurations with energies smaller than U_{\min} . They must have broken spherical symmetry. In our numerical experiments in Section 5, we demonstrate symmetry breaking at a low positive temperature and collapse to aligned degenerate ellipses at an even smaller positive temperature. Before we show these results, we discuss our computational technique in the following section.

4. The Numerical Method

The nonlinear Poisson Equation (11) was solved by TT using various simplifying assumptions and series expansions. In this section, we show that a direct brute force solution of the nonlinear system of Equations (3) and (11) is possible with only minor numerical inventiveness. The numerical method is described below, and the results are given in Section 5.

⁷ We emphasize again that the divergence of the full statistical sum and the existence of the mean-field Poisson–Boltzmann states are not in a one-to-one correspondence. It is possible that the broken-symmetry mean-field thermodynamic equilibria, although they do correctly describe the actual physical states of black hole star clusters, correspond to temperatures below T_c , when the full statistical sum actually diverges. We are working on clarifying this point.

⁸ Not including relativistic precession, which is prograde.

The computations shown in Section 5 require a few-minute calculation on a laptop to find an equilibrium state starting from an arbitrary distribution, and much less time to find a nearby equilibrium. A typical phase-space covering used in our computations was as follows. For parameters A specifying the masses and semimajor axes, we typically use $N_m = 1$ (all stars have the same mass) and $N_a = 30$ possible values of the semimajor axis. For parameters B specifying the orbital ellipses, we use $N_e = 30$ values of eccentricity distributed uniformly in e^2 between zero and 1, $N_1 = 600$ directions of major axes \hat{n}_1 on a Fibonacci spherical lattice, and $N_2 = 30$ perpendicular directions of the minor axes \hat{n}_2 uniformly distributed over the angle of just π , rather than 2π , since an ellipse is traced in both directions in the distribution function given by Equation (3). We represent each ellipse by $N_\xi = 50$ of its points that are uniformly distributed in the eccentric anomaly ξ between zero and 2π and weighted by a factor $\propto (1/P)m dt/d\xi = (2\pi)^{-1}m R/a$. This is done in order to compute the potential energy of the ellipse, as well as the mass density distribution created by all of the ellipses. The gravitational potential and the density are defined on N^3 , $N = 151$, regular spatial grid, and each point representing each ellipse is assigned to a grid cell.

The numerical procedure is as follows. Fix the inverse temperatures β and γ and the distribution function $F(A)$. For finding an equilibrium state for the first time, start with an arbitrary initial potential ϕ . For finding an equilibrium state that is close to the one previously found but with slightly altered parameters, start with the previously calculated potential ϕ . The computation proceeds iteratively by repeating the following steps until the potential ϕ converges (i.e., does not change significantly between successive iterations).

1. Given ϕ : Fix A , calculate the weights $w = e^{-\beta u(A,B)} \cosh[\gamma \cdot j(A, B)]$ for all of the ellipse eccentricities and orientations B , simultaneously calculating the statistical sum $Z(A) = \sum w$. Repeat for all A and obtain $f(A, B)$ from Equation (3); these are the weight factors for the ellipses.
2. Given f : Calculate $\rho(\mathbf{r})$ on the spatial grid by using Equation (12) and replacing the integrals with sums. Calculate several lowest multipoles of ρ ; we found it sufficient to compute the dipole, quadrupole, and octopole moments.
3. Given ρ : Calculate ϕ from the Poisson Equation (11). We have used a simple relaxation method by numerically solving the evolution equation $\partial_{\bar{t}} \phi = \nabla^2 \phi - 4\pi G \rho$, where \bar{t} is the auxiliary time. The boundary conditions at the faces of the computation cube N^3 are given by the multipole expansion of ϕ using the multipoles of ρ computed in the previous step. The size of the cube was chosen to be four times greater than the size of the largest semimajor axis of a star in our sample. The number of \bar{t} steps was chosen so as to make the ρ updating steps (1) and (2) as computationally expensive as the ϕ updating step (3), typically $\sim 1000 \bar{t}$ steps per density update. It takes $\sim N^2 \approx 20,000 \bar{t}$ steps for the potential relaxation procedure to converge. So, the procedure converges after a few dozen density updates.

The numerical convergence was tested by (1) repeating the calculations at different resolutions, (2) comparing the numerical results to a few analytically doable calculations, and (3)

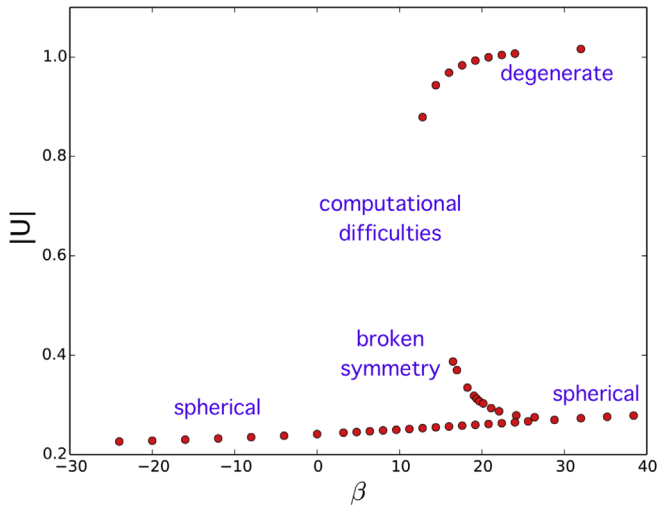


Figure 1. Thermodynamic equilibria in the $\beta - |U|$ plane for a nonrotating cluster. The cluster is made of stars with the same mass m_0 , with the total cluster mass M_{cluster} and semimajor axes uniformly distributed in the interval $(a_0, 2a_0)$. Here $|U|$ is in units of $GM_{\text{cluster}}^2/a_0$, and β is in units of $(GM_{\text{cluster}}m_0/a_0)^{-1}$.

comparing the numerical results to high-resolution spherically symmetrical numerical results, as explained in the next section.

5. The Numerical Results

The numerical results described here (1) demonstrate the existence of both rotating and nonrotating equilibria with symmetry breaking, (2) give supporting evidence for the existence of the high- β singularity and associated degenerate states, and (3) show an important effect: that massive objects such as stellar-mass black holes occupy special orbits in the clusters.

The examples shown in this section use mostly single-mass m_0 star clusters with the uniform distribution of semimajor axes $a_0 < a < 2a_0$. When stellar-mass black holes are introduced, their mass is $10m_0$. The inverse temperature β is measured in units of $(GM_{\text{cluster}}m_0/a_0)^{-1}$, γ is measured in units of $(\sqrt{GMa_0}m_0)^{-1}$, the binding energy $|U|$ is measured in units of $(GM_{\text{cluster}}^2/a_0)$, and the dipole moment d is measured in units of $M_{\text{cluster}}a_0$.

5.1. Nonrotating Clusters

Figure 1 shows the equilibria for nonrotating clusters we were able to find. For each β , different solutions of the nonlinear Poisson equation are represented by their gravitational binding energy $|U|$. There are several notable features on this plot.

The lower branch represents spherically symmetric clusters, with the left end (low β and binding energy) featuring very eccentric orbits and the right end (high β and higher binding energy) featuring orbits close to circular. A projected density profile of two examples of the spherical equilibria is shown in Figures 2 and 3. The energy of spherical clusters with purely circular and radial orbits can be computed analytically, and we checked that these values are in good agreement with the asymptotic values on our plot. Our procedure for exploring this branch was as follows. We start with a small inverse temperature $\beta \ll -1$ and choose a spherically symmetrical initial potential ϕ , say $\phi = 0$, and the program soon saturates in a spherically symmetrical thermodynamic equilibrium with very eccentric

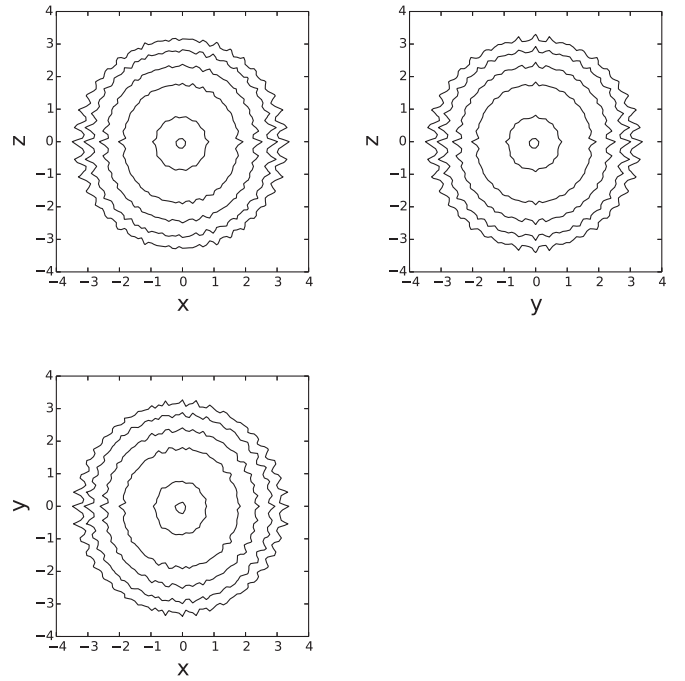


Figure 2. Spherical low- β “hedgehog” state. The stars are on eccentric orbits. Projected surface density for $\beta = -24.0$, $\gamma = 0$, $|U| = 0.226$. The isolines are 0.025, 0.05, 0.1, 0.2, 0.4, and 0.8 of the maximal projected surface density. The ruggedness is due to the finite number of ellipse orientations (600) used in the numerical procedure.

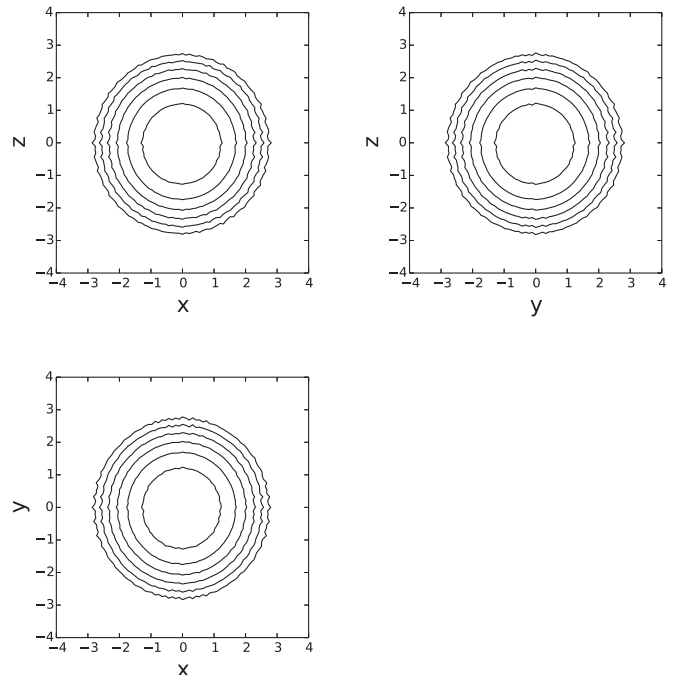


Figure 3. Spherical high- β circular-orbit state. Projected surface density for $\beta = 35.7$, $\gamma = 0$, $|U| = 0.276$.

orbits. We then increase β gradually and use the potential computed in the previous step as an initial potential for our iterative procedure described in the previous section. We have also written an independent code that computes equilibria with enforced spherical symmetry (and thus has very high resolution), and we checked that the energy values agree between the two codes. When we reach the maximum value of $\beta \simeq 40$, the

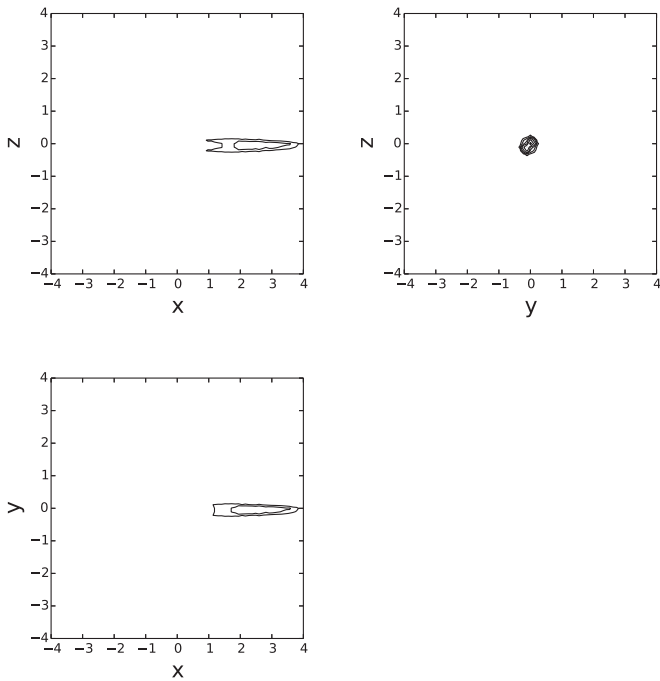


Figure 4. Degenerate state. Projected surface density for $\beta = 12.8$, $\gamma = 0$, dipole moment $d = 2.12$, $|U| = 0.88$.

algorithm fails to find a spherically symmetric equilibrium; instead, the solution jumps to the upper branch that we mark as “degenerate.” As shown in Figure 4, the orbits in this state are nearly radial and strongly aligned, with needlelike projected surface density. We believe that this state represents the high- β singularity identified in Section 3; obviously, with our numerical resolution, we do not obtain $|U| = \infty$. The dipole moment of the degenerate branch is displayed in Figure 5 to be close to the theoretical maximum value of $9/4$, obtained for perfectly aligned degenerate ellipses with axes uniformly distributed between 1 and 2. We follow the degenerate branch to the left by decreasing β in steps and using the potential from the previous step as an initial potential for the iterative procedure. Once we reach the leftmost point, the solution jumps back down to the spherical branch. We have checked that the actual U values for the degenerate branch are very strongly resolution-dependent, as they should be.

Of particular interest is the branch that bifurcates upward at $\beta \simeq 30$ and $|U| \simeq 0.27$ from the spherical branch. These are the nondegenerate states with broken symmetry. Two examples of such states are shown in Figures 6 and 7. These equilibria are difficult to find, since for a fixed β and arbitrary initial potential, the solution tends to converge onto the upper or lower branch. Instead of fixing β , we introduced a feedback loop, where we changed β every iterative step depending on the current value of the dipole moment or the binding energy $|U|$. The basic idea is that if the dipole moment becomes large, we reduce β , and if it becomes small, we increase it. To obtain the results shown in Figure 1, we used the following prescription found by trial and error: $\beta_i = 40 - c d_{i-1}$, where i is the index labeling the iterations, d_{i-1} is the dipole moment obtained in the previous iteration, and c is a constant. Starting with $c \simeq 20$ and initial ϕ with $|\nabla\phi| \simeq 1$, we get a convergent solution that satisfies the extra constraint $\beta = 40 - c d$. Then, by varying c , we obtain part of the nondegenerate broken-symmetry branch that is shown in the figure. We emphasize that the presence of

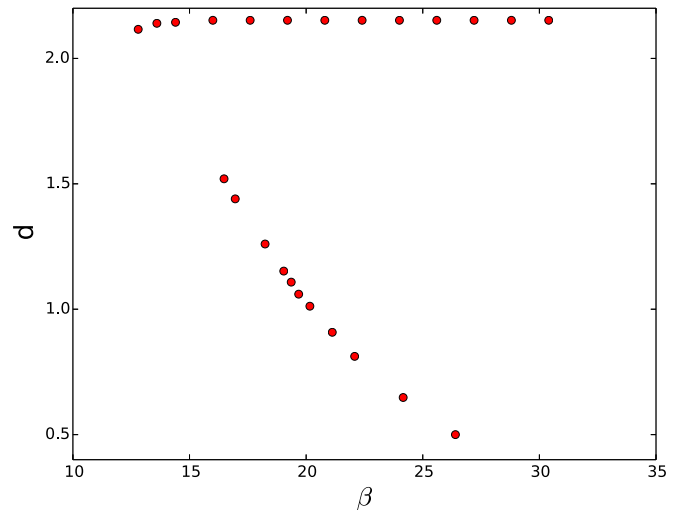


Figure 5. Dipole moment of states with broken symmetry and of degenerate states. Measured in units of $M_{\text{cluster}} a_0$, the maximum possible value is 2.25.

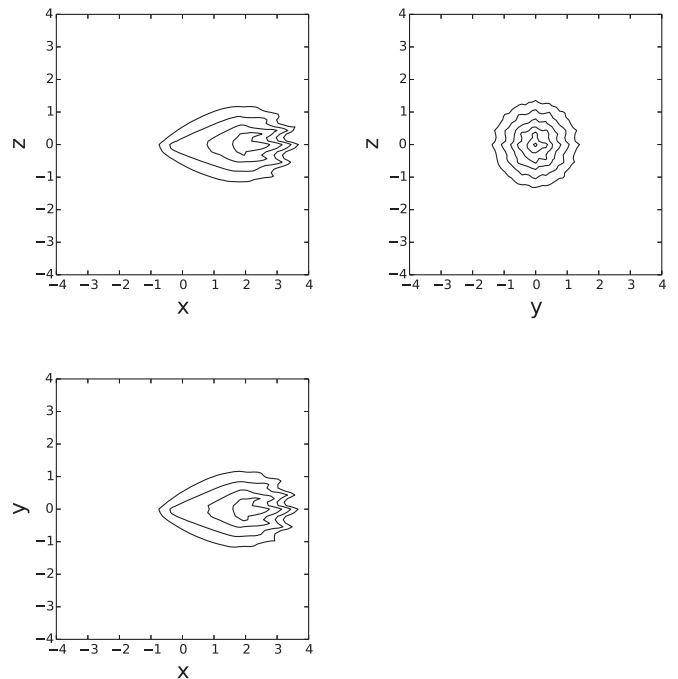


Figure 6. Projected surface density of a nonrotating cluster in a lopsided equilibrium for $\beta = 16.5$, $\gamma = 0$, $d = 1.51$, and $|U| = 0.387$.

the feedback loop does not change the fact that the program finds a solution of the nonlinear Poisson Equations (3) and (11), because the program does saturate, meaning that the inverse temperature ultimately becomes a constant. This procedure allowed us to find equilibria with broken symmetry with binding energies up to $|U| = 0.40$, but the algorithm failed to converge for higher energies. We know from Section 3 that equilibria with arbitrarily high binding energies must exist; therefore, we conclude that our failure to find such equilibria is due to computational difficulties and does not reflect a matter of principle.

It is important to remember that a cluster we are considering is represented by a microcanonical ensemble with conserved binding energy $|U|$. There is a range of values, $0.27 \lesssim |U| < 1 - \ln 2 \approx 0.31$ (the theoretical maximum binding energy of a spherical

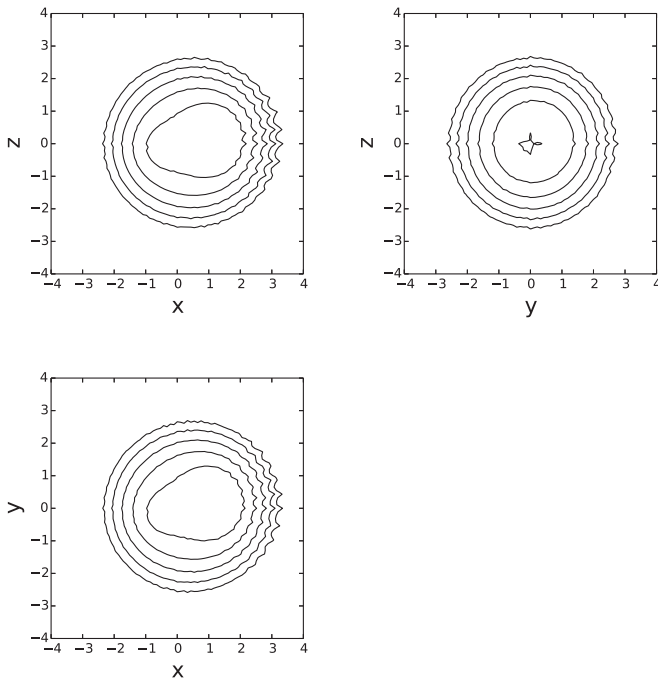


Figure 7. Projected surface density of another nonrotating cluster in lopsided equilibrium for $\beta = 25.6$, $\gamma = 0$, $d = 0.552$, $|U| = 0.276$.

cluster), where we are finding solutions with two possible values of β , one spherically symmetric and one with broken spherical symmetry. It is likely that one of these solutions is metastable (like overheated water or overcooled water vapor) or unstable. Intuitively, it seems likely that since the broken-symmetry state has a higher temperature, it occupies a greater volume of phase space. Therefore, it is the broken-symmetry state that is stable. This argument is in harmony with the results of Tremaine (2005), who showed that spherically symmetric clusters with preferentially circular orbits are subject to secular-dynamical instability.

Finally, it is interesting to note that the clusters on the broken-symmetry branch have negative heat capacity. This can potentially lead to thermogravitational instability if the cluster comes into contact with the heat bath at the same temperature (how this would be implemented in practice is another matter); presumably, in this case, the cluster would collapse to a degenerate state.

5.2. Rotation

Figure 8 shows an example of a lopsided equilibrium of a rotating cluster. The orbits are eccentric, and their eccentricities are strongly aligned with each other. Notably, the surface density in the equatorial plane shows two enhancements: one near the supermassive black hole due to the clustering of the stars at small radii due to their a -distribution, and the other due to clustering of the apocenters of orbital ellipses. The nuclear cluster in Andromeda has similar structure, which led Tremaine (1995) to model it as an “eccentric disk.” The disk consists of old stars (Bender et al. 2005) and is likely dynamically old, so one may expect it to reach secular-dynamical equilibrium. It would therefore be of interest to fit the data in Andromeda using the rotating lopsided equilibria that we are finding; this is a subject for future work. We note that rotating nuclear star clusters often coexist with supermassive black holes (Seth et al. 2008; Graham & Spitler 2009); thus, there are reasons to think that eccentric disks are common.

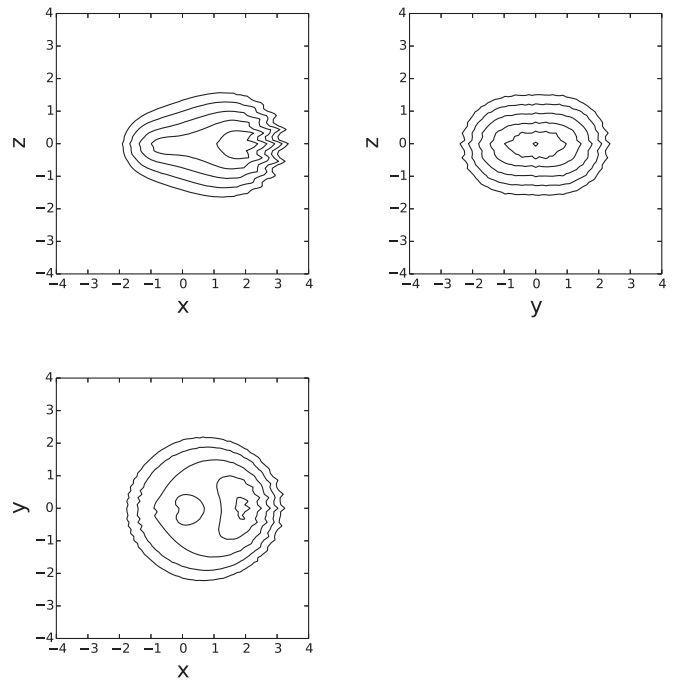


Figure 8. Projected surface density of a rotating stellar cluster in lopsided equilibrium, with $\beta = 23.0$, $\gamma = 2.30$, $d = 0.944$, and $|U| = 0.321$.

We can find the lopsided rotating equilibria by starting with the nonrotating lopsided equilibrium with $\gamma = 0$ and then slowly switching on the rotation by incrementally increasing γ . We find that for sufficiently rapid rotation, the cluster becomes axially symmetric; this must take place when the angular velocity of the cluster $\Omega = \gamma/\beta$ exceeds the possible angular velocity of the precession of elliptical orbits of the cluster. An example of an axisymmetric rotating cluster is shown in Figure 10.

5.3. Stellar-mass Black Holes

It is of great astrophysical interest to consider the orbits of heavy objects in a black hole cluster, such as those of stellar-mass black holes. In thermodynamics, heavy particles occupy the lowest available potential energy states. This, however, is only true for positive temperatures, so we should be careful; for negative temperatures, the opposite is true. Moreover, extending our intuition from β to γ , we may expect that stellar-mass black holes will maximally align their angular momenta with the latter.

The lopsided equilibria of the previous subsections take place at positive temperatures; therefore, black holes will tend to adjust their orbits to minimize their potential energies. This means that their eccentricity vectors are expected to be strongly aligned with the lopsidedness of the potential, and their density distribution should be more lopsided than that of the lighter stars. This is demonstrated in Figure 9.

To demonstrate the orbital angular momentum alignment, in Figure 10, we show the black hole subcluster of a rotating axisymmetric cluster. While the cluster is only mildly flattened by the rotation, the black hole orbits condense into a disk. This interesting behavior of black holes in rotating nuclear clusters was predicted by Szölygyén & Kocsis (2018) using a different technique and is discussed in some detail in the next section.

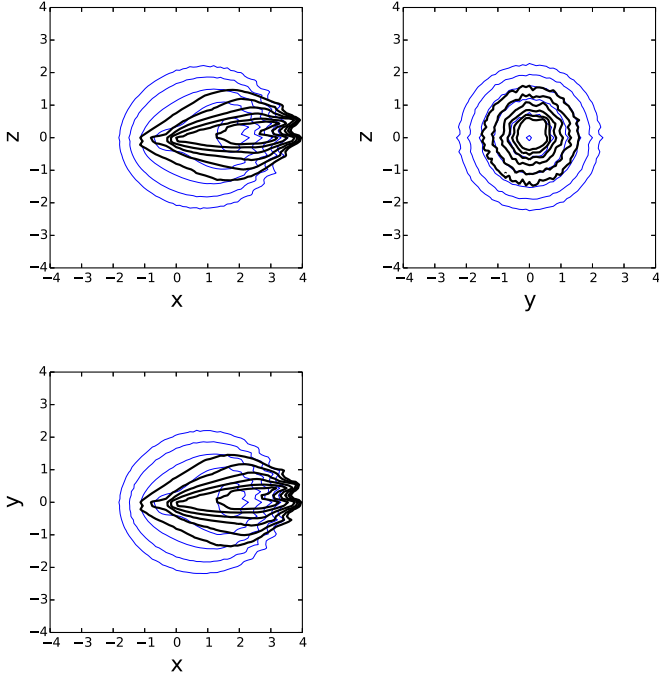


Figure 9. Nondegenerate broken-symmetry state with stellar-mass black holes with masses of $10m_0$. The black holes are on more eccentric orbits than the background stars. The thin blue lines indicate background stars. The thick black lines indicate stellar-mass black holes. The projected surface density is plotted for $\beta = 20.6$, $\gamma = 0$, $d = 0.972$, and $|U| = 0.298$.

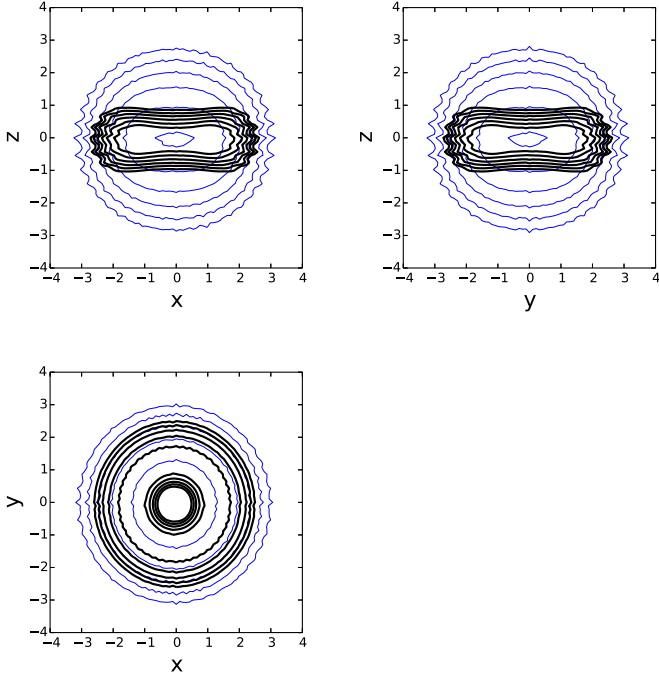


Figure 10. Axially symmetrical rotating state with stellar-mass black holes. The black holes are concentrated near the equator on more circular orbits. The projected surface density is plotted for $\beta = 0$, $\gamma = 2.30$, $d = 0.092$, and $|U| = 0.252$. The projected surface density of a stellar-mass black hole subcluster inside a rotating axisymmetric cluster is plotted in black.

6. Orbits of Stellar-mass Black Holes: Analytical Treatment

At the end of the previous section, we saw that stellar-mass black holes are very sensitive “thermometers” of the clusters; their orbital eccentricity and rotation are strongly amplified

compared to the lighter members of the cluster for those clusters that have broken symmetry or are rotating. It is possible to gain an analytical handle on this property of the stellar-mass black holes by considering several limiting cases.

6.1. Spherical Clusters

We explore the case when the background cluster is spherically symmetric and contains a large number of stars. In this case, the overall potential per unit mass has a dominant spherically symmetric smooth component $\phi(r)$, where r is the distance to the supermassive black hole at the center. The fluctuating nonspherical part of the potential leads to the exchange of energy between different orbits and drives the system to thermodynamic equilibrium. However, only the smooth component is contributing when evaluating the Boltzmann weights.

We will consider general spherical clusters and, for concreteness, the special case of self-similar (power-law density) clusters. To understand the behavior of heavy stars, we need to analyze the properties of the mean potential energy of an orbit in Equation (5). It is given by

$$u(m, a, l) = \frac{m}{2\pi a} \int_0^{2\pi} \phi[R(l, \xi)]R(l, \xi)d\xi, \quad (19)$$

where

$$R = a[1 - \sqrt{1 - l^2} \cos(\xi)] \quad (20)$$

is the radius. Here $l = \sqrt{1 - e^2} = j(GMm^2a)^{-1/2}$ is the dimensionless angular momentum of the orbit. Consider self-similar spherical clusters with a power-law density distribution

$$\rho(r) = Cr^{-\delta}, \quad (21)$$

where C is a constant and δ is typically between 1.25 and 1.75. The potential is then

$$\phi(r) = \frac{4\pi GC}{(3 - \delta)(2 - \delta)} r^{2-\delta}. \quad (22)$$

The orbit-averaged potential energy is given by

$$u(m, a, l) = \frac{4\pi mGC a^{2-\delta}}{(3 - \delta)(2 - \delta)} l^{3-\delta} P_{3-\delta}(1/l), \quad (23)$$

where P_μ is the Legendre function. Since the order of the Legendre function is typically noninteger, the expression above is neither intuitive nor very useful. We found it more convenient to expand it in powers of l^2 . For example, for the Peebles–Young cusp with $\delta = 1.5$, an excellent approximation is

$$u(m, a, l) = \frac{16\pi mGC a^{0.5}}{3} \times \left[\frac{8\sqrt{2}}{3\pi} - \frac{1}{\pi\sqrt{2}} l^2 + 0.0247 l^4 \right]. \quad (24)$$

The first two terms on the right-hand side are obtained analytically from the Taylor series, while the third term was chosen to match the exact expression at the maximum value of $l = 1$. The overall approximation has a fractional accuracy better than 3×10^{-3} for all l .

The quadratic dependence on l for small values of l holds for general spherically symmetric clusters and follows directly

from Equation (19). One can show that for $l \ll 1$,

$$u(m, a, l) = u_0(m, a) - \frac{1}{2} \left(\frac{GMm}{a} \right) \alpha l^2. \quad (25)$$

Here the dimensionless coefficient α is positive for $\phi(R)$ created by a stellar cluster and given by the following expression:

$$\alpha = \frac{a}{GM} \frac{1}{\pi} \int_0^\pi \frac{d\phi[R(\xi)]}{dR} R(\xi) d\xi, \quad (26)$$

where $R(\eta) = a[1 - \cos(\xi)]$ follows that of the radial orbit with semimajor axis a . For the potential given by Equation (22),

$$\alpha = \frac{4\pi C a^{3-\delta} 2^{2-\delta} \Gamma(2.5 - \delta)}{M(3 - \delta) \sqrt{\pi} \Gamma(3 - \delta)}. \quad (27)$$

It is instructive to write the above equation in terms of $M_{\text{cluster}}(<a)$, the mass in stars at radii less than a :

$$\alpha = q(\delta) \frac{M_{\text{cluster}}(<a)}{M}, \quad (28)$$

where

$$q(\delta) = \frac{2^{2-\delta} \Gamma(2.5 - \delta)}{\sqrt{\pi} \Gamma(3 - \delta)}. \quad (29)$$

In the range of interest, the numerical prefactor q is not a sensitive function of δ , and it approximately equals 0.9 for $\delta = 1.5$.

It is now straightforward to write down the probability distribution function for an orbit with a semimajor axis a and mass m to have a square eccentricity $e^2 = 1 - l^2$:

$$\mathcal{P}_{a,m}(e^2) = \frac{1}{N_0} \exp[-\beta u(m, a, l)], \quad (30)$$

where

$$N_0 = \int_0^1 d(l^2) \exp[-\beta u(m, a, l)] \quad (31)$$

is the normalization factor.

For fixed a and m , the variation of $u(m, a, l)$ is approximately given by

$$u(m, a, 0) - u(m, a, 1) \sim \alpha \frac{GMm}{2a}, \quad (32)$$

where α is given by Equation (26); for the power-law cluster, α is given by Equation (28). Therefore, the character of the l distribution (and therefore the character of the eccentricity distribution) is determined by a dimensionless parameter,

$$\bar{\beta}(m, a) = \frac{\beta GMm \alpha}{2a}. \quad (33)$$

There are three limiting cases.

Case 1: $|\bar{\beta}| \ll 1$. In this high-temperature limit, the distribution is uniform in the l^2 , and

$$\begin{aligned} \mathcal{P}(l) &= 2l \\ \mathcal{P}(e) &= 2e. \end{aligned} \quad (34)$$

For historical reasons, this is called the ‘‘thermal’’ distribution of eccentricities and angular momenta. In fact, a more accurate name is the maximum-entropy distribution. While it is assumed to hold for relaxed clusters in much of the literature on resonant

relaxation, we emphasize that it is really the high-temperature subset of possible thermal equilibria. For $\bar{\beta} < 0$, i.e., for negative temperature, the values of l will, on average, be lower than those of the distribution in Equation (34), and thus the orbits will be more eccentric. Conversely, for $\bar{\beta} > 0$, i.e., for positive temperature, the orbits will, on average, be less eccentric than those in Equation (34). The other two limiting cases are as follows.

Case 2: $\bar{\beta} \ll -1$. In this low negative temperature limit, the orbits are eccentric and the distribution is exponential in l^2 , given by

$$\mathcal{P}(l^2) \simeq |\bar{\beta}| \exp[-|\bar{\beta}| l^2]. \quad (35)$$

The associated mean values are

$$\begin{aligned} \langle l^2 \rangle &= |\bar{\beta}|^{-1} \\ \langle e^2 \rangle &= 1 - |\bar{\beta}|^{-1}. \end{aligned} \quad (36)$$

The analysis in this paper and in TT shows that such ‘‘hedgehog’’ clusters are stable.

Case 3: $\bar{\beta} \gg 1$. In this low positive temperature limit, the orbits are nearly circular (tangential). The computations in TT and this paper suggest that the clusters with preferentially tangential orbits are unstable and develop strongly lopsided structures.

Power-law cusps. Consider as a useful example the power-law cusp, with α given by Equation (27). In that case,

$$\begin{aligned} \bar{\beta}(a) &= \beta Gm C a^{2-\delta} \frac{\sqrt{\pi} 2^{3-\delta} \Gamma(2.5 - \delta)}{(3 - \delta) \Gamma(3 - \delta)} \\ &= \frac{\beta}{|\bar{\beta}|} \frac{m}{m_0} \left(\frac{a}{a_{\text{th}}} \right)^{2-\delta}, \end{aligned} \quad (37)$$

where m_0 is the mass of a typical star in the cluster, and

$$a_{\text{th}} = \left[|\bar{\beta}| Gm_0 C \frac{\sqrt{\pi} 2^{3-\delta} \Gamma(2.5 - \delta)}{(3 - \delta) \Gamma(3 - \delta)} \right]^{\frac{1}{\delta-2}} \quad (38)$$

is the semimajor axis at which $|\bar{\beta}| = 1$ for a star of mass m_0 . We see immediately that for $a \ll a_{\text{th}}$, the orbits of stars with mass m_0 are following the maximum-entropy distribution of Equation (34). For $a > a_{\text{th}}$, the orbits are becoming more eccentric as a increases if the temperature is negative. For positive temperature, the orbits become more circular as a increases, and the cluster is likely to develop a lopsided configuration beyond some critical radius, thus breaking the spherical symmetry.

Heavy objects inside spherical clusters. Black holes, as well as massive stars, likely exist inside nuclear star clusters, and their masses can be much greater than those of the majority of the cluster members. From Equation (37), we see that the dimensionless temperature parameter $\bar{\beta}$ scales linearly with the mass of the object. The heavy objects will have a different eccentricity distribution than the majority of the stars with the same semimajor axes. In fact, for $\delta = 1.5$, a black hole with a mass 10 times greater than the average stellar mass will have the same eccentricity distribution as the majority of the stars with semimajor axes 100 times greater than the black hole’s.

In other words, for a negative-temperature cluster, heavy objects are on more eccentric orbits than their neighbors; this is the effect that was likely seen in the numerical experiments of

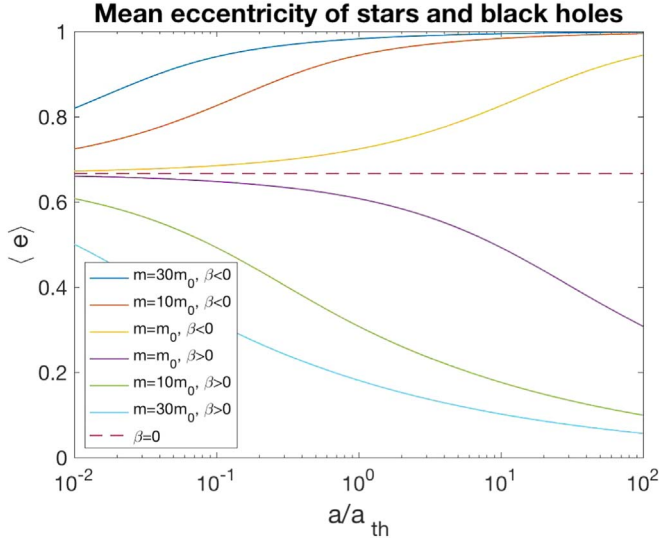


Figure 11. Mean eccentricity as a function of radius for a power-law cluster with $\delta = 1.5$, plotted for populations with three characteristic masses: $m = m_0$ (the background stars), $10m_0$, and $30m_0$ (the black holes and massive stars).

Madigan & Levin (2012). Conversely, for positive temperatures (if the cluster is still stably spherical), the heavy objects are on less eccentric orbits than their neighbors. The effect can be quite dramatic, as illustrated in Figure 11, where mean eccentricities are plotted for stars and black holes in a power-law cluster with $\delta = 1.5$. We see that if the mean eccentricity of the stars exceeds that of the maximum-entropy distribution, the orbits of black holes and other heavy objects are substantially more eccentric than those of the rest of the stars, on average. Conversely, if the orbits of the background stars are more circular, on average, than $e = 2/3$, then the orbits of black holes and other heavy objects are substantially more circular than those of the background stars.

The eccentricity of the black hole orbits is a sensitive thermometer for the rest of the stellar distribution. We can see near $a = a_{\text{th}}$, where the background distribution deviates very slightly from the maximum-entropy one, that heavy black holes dramatically amplify these deviations. Clearly, this will have major consequences for the interaction of heavy objects with the supermassive black hole, since these interactions require the heavy object to acquire an extremely eccentric orbit. We will postpone a detailed discussion of such interactions to future work, since they require understanding of not just an equilibrium distribution but also the stochastic evolution of the orbits.

6.2. Rotation

Rotation impacts the distribution of stellar orbits in two ways. It introduces a second temperature-like parameter $\vec{\gamma}$ that enters into the Boltzmann weight through a factor $\exp[\vec{\gamma} \cdot \mathbf{j}]$. This extra factor creates a preference for the angular momenta of the stars to be aligned with $\vec{\gamma}$. Rotation also flattens the cluster toward its equatorial plane via the direction-averaged Boltzmann factor $\cosh[\vec{\gamma} \cdot \mathbf{j}]$. Since $j \propto m$, stellar-mass black holes' angular momenta are much stronger aligned than those of the rest of the stars, and as we saw in Section 5, for realistic parameters, they form disklike configurations inside rotating clusters.

Without loss of generality, we choose the z -axis to be aligned with $\vec{\gamma}$. We work with Delaunay action-angle variables for Keplerian orbits with fixed semimajor axes, with actions j, j_z and corresponding angles ζ, ζ_z . Here ζ_z is the angle of the line of nodes,⁹ and ζ is the argument of the periastron.¹⁰ The probability distribution function for a star with fixed a, m is given by

$$\mathcal{P}_{a,m}(j, j_z, \zeta, \zeta_z) = \frac{1}{N_2} \exp[-\beta u(m, a, j, j_z, \zeta, \zeta_z) + \gamma j_z]. \quad (39)$$

Here, as always, u is the orbit-averaged energy, j is restricted to vary between zero and $j_c = m\sqrt{GMa}$, j_z is restricted to vary between $-j$ and j , and N_2 is the normalization.

In general, the potential energy u has to be computed numerically, as was done in Section 5. To gain intuition from an analytical calculation, we consider three limiting cases.

Case 1: heavy black holes with $m \gg m_0$. Since both u and j scale linearly with m , such black holes will cluster around the orbit that maximizes the function

$$p(j/m, j_z/m, \zeta, \zeta_z) \equiv (1/m)[\gamma j_z - \beta u]. \quad (40)$$

This implies that $\partial u / \partial \zeta = 0$ and $\partial u / \partial \zeta_z = 0$, so the orbit experiences no torque along \mathbf{j} or the z -axis. If the orbit is inclined, the torque

$$\boldsymbol{\tau} \propto \hat{\mathbf{z}} \times \mathbf{j} \quad (41)$$

and the angular momentum vector \mathbf{j} precesses around the z -axis. How quickly would it precess? The inclined orbit implies $|j_z| < j$, so maximizing p with respect to j_z gives

$$\frac{\partial u}{\partial j_z} = \Omega. \quad (42)$$

The left-hand side is the rate of precession of the line of nodes in the $x - y$ plane. Maximizing p with respect to j implies that either $j = j_c$ and the orbit is circular or $\partial p / \partial j = 0$ and ζ is constant. In either case,¹¹ the orbit is stationary in the frame of reference rotating with Ω .

If the orbit is located in the equatorial plane, $j_z = j$ (for simplicity, we can choose the direction of the z -axis to fix the plus sign). Maximizing p with respect to j implies that either the orbit is circular or

$$\frac{\partial u(m, a, j, \zeta)}{\partial j} = \Omega. \quad (43)$$

Here ζ is the argument of the periastron in the equatorial plane (relative to, e.g., the x -axis). The orbit is either circular or precesses with angular velocity Ω in the equatorial plane. Therefore, we generally proved that heavy black holes are attracted to orbits that are stationary in the frame of reference rotating with angular frequency Ω .

Case 2: infinite-temperature cluster ($\beta = 0$). The mathematics becomes fully analytical; the angles ζ, ζ_z drop out, and

⁹ A common term in celestial mechanics, signifying the angle between the x -axis and the line of intersection between the orbital and $x - y$ planes.

¹⁰ The angle between the line of nodes and the radial line through the periastron of the orbit.

¹¹ At first glance, it seems logically possible that p could be maximized at $j = j_z = 0$. However, recall that $\partial u / \partial j = 0$ at $j = 0$; therefore, this cannot be a maximum of p when γ is not zero.

we get

$$\mathcal{P}_{a,m}(j, j_z) = \frac{\gamma^2 e^{\gamma j_z}}{2[\cosh(\gamma j_c) - 1]} \quad (44)$$

for $0 \leq j \leq j_c$ and $-j \leq j_z \leq j$ and zero otherwise. The inclination angle of the orbit $0 \leq \theta \leq \pi$ is given by $c \equiv \cos \theta = j_z/j$, and

$$\begin{aligned} \mathcal{P}_{a,m}(c) &= \int_0^{j_c} dj \int_{-j}^j dj_z s_{\text{cr}} \mathcal{P}_{a,m}(j, j_z) \delta(j_z/j - c) \\ &= \frac{1 + e^{\bar{\gamma}c}(\bar{\gamma}c - 1)}{2(\cosh \bar{\gamma} - 1)c^2}, \end{aligned} \quad (45)$$

where $\bar{\gamma} = \gamma j_c$ fully determines the distribution of inclinations. For slow rotation, $\bar{\gamma} \ll 1$ and $\mathcal{P}(c) = 1/2$, which corresponds to isotropically distributed orbits. For rapid rotation, $\bar{\gamma} \gg 1$ and the values of c are concentrated near 1, with the probability density approximately given by

$$\mathcal{P}_{a,m}(c) \simeq \bar{\gamma} e^{-\bar{\gamma}(1-c)}. \quad (46)$$

In this limit, the inclination angles are concentrated near zero, their probability density is given by

$$\mathcal{P}_{a,m}(\theta) \simeq \bar{\gamma} \theta e^{-\frac{1}{2}\bar{\gamma}\theta^2}, \quad (47)$$

and the mean value of the inclination is given by

$$\langle \theta \rangle \simeq \sqrt{\frac{\pi}{2\bar{\gamma}}}. \quad (48)$$

Note that the mean inclination angle is weakly decreasing with the semimajor axis, $\langle \theta \rangle \propto a^{-1/4}$, and more sensitively decreasing with the black hole mass, $\langle \theta \rangle \propto m^{-1/2}$. Finally, we note that rotation makes the orbits more circular, on average, with

$$\mathcal{P}_{a,m}(l) = \frac{\bar{\gamma} \sinh[\bar{\gamma}l]}{\cosh \bar{\gamma} - 1}. \quad (49)$$

For $\bar{\gamma} \gg 1$, the eccentricity values cluster around zero, with the probability distribution function

$$\mathcal{P}_{a,m}(e) \simeq \bar{\gamma} e \exp\left[-\frac{1}{2}\bar{\gamma}e^2\right], \quad (50)$$

and the mean value of the eccentricity is the same as that of the inclination:

$$\langle e \rangle \simeq \sqrt{\frac{\pi}{2\bar{\gamma}}}. \quad (51)$$

Case 3: nearly spherical cluster with rotation. We saw in the previous paragraph that rotation makes the orbital distribution more circular, on average. This effect was demonstrated for $\beta = 0$ and is expected to be suppressed or enhanced for $\beta < 0$ or $\beta > 0$, respectively. To study this, we assume that both β and γ are nonzero but that the potential is spherically symmetric and given by Equation (22). We must keep in mind that this approximation is not self-consistent for rapidly rotating clusters with high γ , but it does give us a qualitative picture of the effect of the two temperatures on the distribution of black hole orbits. Furthermore, we specify the density profile to $\delta = 1.5$, with the orbit-averaged energy $u(m, a, l)$ given by Equation (25).

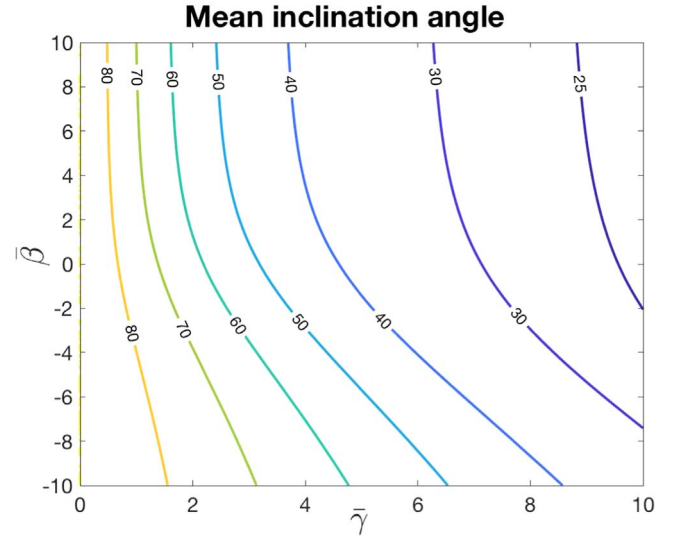


Figure 12. Mean inclination of orbits as a function of $\bar{\beta}$ and $\bar{\gamma}$ for a rotating cluster with $\delta = 1.5$. Both parameters scale linearly with mass, so stellar-mass black holes tend to have high $\bar{\gamma}$, and their orbits strongly align with the rotation of the cluster.

With these assumptions, the probability density distribution for $(l, l_z) = (j/j_c, j_z/j_c)$ becomes

$$\mathcal{P}_{a,m}(l, l_z) = \frac{1}{N_1} \exp[\bar{\beta}(l^2 - 0.11 l^4) + \bar{\gamma}l_z], \quad (52)$$

where N_1 is the normalization factor and $\bar{\beta}$ is given by Equation (37). It is worth emphasizing that for a given power-law exponent δ of the cluster's density profile, the probability distribution function with respect to l, l_z is completely specified by the dimensionless temperature and rotation parameters $\bar{\beta}$, given by Equation (33), and $\bar{\gamma}$. The probability distribution above the peaks for aligned orbits with $l_z = l$, which are circular ($l = 1$) if $\bar{\beta} \geq -0.64\bar{\gamma}$ and eccentric and precessing with the cluster's angular velocity,

$$\Omega = \frac{\alpha\bar{\gamma}}{2\bar{\beta}} \sqrt{\frac{GM}{a^3}}, \quad (53)$$

if $\bar{\beta} < -0.64\bar{\gamma}$. In Figures 12 and 13, we show the mean inclination and eccentricity of the orbits as a function of $\bar{\gamma}$ and $\bar{\beta}$ computed for a cluster with $\delta = 1.5$. We can see that the rotational vector γ biases the orbital angular momenta to be coaligned with it, and in the high- $\bar{\beta}$ case, the orbits are particularly susceptible to this coalignment. Since $\bar{\gamma}$ scales with the mass of the star, the orbits of heavy stars and black holes will align their angular momenta with $\bar{\gamma}$ even for modest rotations of the background clusters. We believe this argument is consistent with the “black hole disks” seen in recent Monte Carlo simulations with circular orbital annuli by Szölgvény & Kocsis (2018). Figure 14 illustrates the degree of alignment of black hole orbits with the cluster rotation vector as a function of the black hole mass. As the latter is increased, the orbits get locked into the equatorial plane, as expected.

6.3. Planets, Comets, and Other Light Particles

Of some astrophysical interest is the dynamics of the very light particles (as compared to the stars) that might be present in galactic nuclei. Nayakshin et al. (2012) argued that

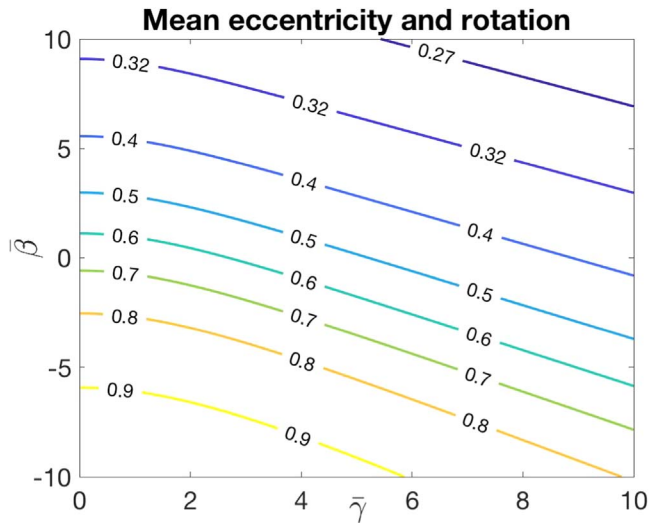


Figure 13. Mean eccentricity of the orbits decreases with rotation, which can have an effect on the interaction of stars and stellar-mass black holes with the supermassive black hole at the center of the cluster.

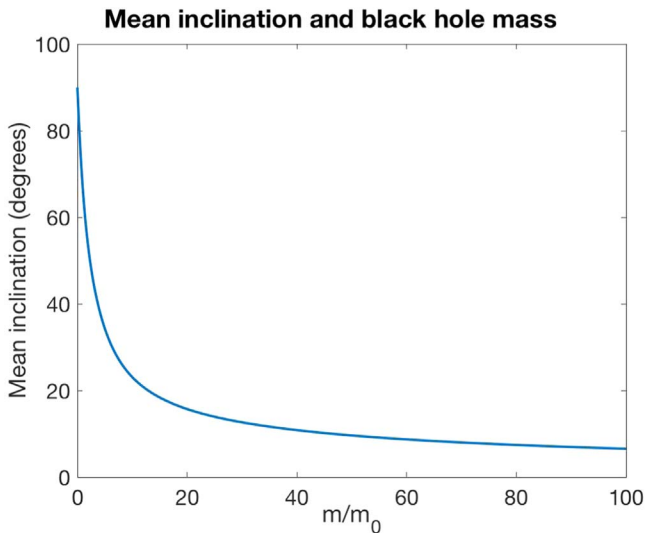


Figure 14. Mean inclination of a black hole as a function of its mass for $\bar{\gamma} = -\bar{\beta} = 2(m/m_0)$.

supermassive black holes are surrounded by swarms of comets and asteroids. Gondolo & Silk (1999) showed that the growth of a supermassive black hole naturally leads to a dark matter spike in its vicinity. In both cases, the total mass of the light particles is subdominant to that of the stars surrounding the black hole, and their gravitational dynamics is determined by that of the stars. Since $\bar{\beta}$ and $\bar{\gamma}$ scale linearly with the mass, $\bar{\beta} = \bar{\gamma} = 0$ is a very good approximation. Therefore, the light particles are expected to form a spherical subcluster with no observable rotation, regardless of how rapidly the stellar cluster rotates and how asymmetric it is. They follow the maximum-entropy distribution in eccentricities, $s_{\text{cr}}P(e) = 2e$. This remarkable simplicity should be of use for studies exploring the observational signatures of light objects in galactic nuclei.

7. Conclusions

Touma–Tremaine thermodynamics is a powerful tool for describing the secular-dynamical equilibria of stellar clusters

near supermassive black holes. In this paper, we give a general analytical and numerical treatment of thermal equilibria for both nonrotating and rotating clusters. We show that the existence of lopsided equilibria is robust and argue that the eccentric nuclear disk of Andromeda is likely an example of thermal equilibrium in a rotating precessing cluster.

We argue that heavy stellar-mass black holes are sensitive “thermometers” of the clusters and are attracted to a special set of orbits. For spherical nonrotating clusters, they are either much more or much less eccentric than the lighter stars, depending on the sign of the temperature. In rotating clusters, they tend to form disklike structures, as was previously argued by Szölglyén & Kocsis (2018) by carrying out Monte Carlo simulations with circular orbital annuli. Consistent with this, preferentially low inclinations for heavy stars were observed by Foote et al. (2020) in their simulations of an eccentric disk. Additionally, we show that black hole orbits tend to be stationary in a frame of reference rotating with the cluster’s angular velocity. In lopsided clusters, their eccentricity vectors tend to be lined up with the direction of asymmetry of the cluster, more so than those of the lighter stars. Importantly, cluster rotation tends to deplete strongly eccentric orbits and may reduce the number of stars and especially black holes interacting with the supermassive black hole. This could have a profound impact on the tidal disruption events and gravitational wave–driven inspirals of stellar-mass black holes in galactic nuclei. These topics will be explored in future work.

On the other end of the mass spectrum, we remark that comets, asteroids, and dark matter particles form a spherically symmetric nonrotating subcluster inside a generally rotating and possibly lopsided black hole cluster. This nonintuitive statement is an immediate consequence of Touma–Tremaine thermodynamics and should inform studies of observational signatures of such light objects in galactic nuclei.

We thank Scott Tremaine for numerous insightful discussions on stellar dynamics in galactic nuclei and Jihad Touma for useful feedback on the draft of this paper.

References

- Bar-Or, B., & Alexander, T. 2016, *ApJ*, 820, 129
 Bar-Or, B., & Fouvy, J.-B. 2018, *ApJL*, 860, L23
 Bender, R., Kormendy, J., Bower, G., et al. 2005, *ApJ*, 631, 280
 Foote, H. R., Generozov, A., & Madigan, A.-M. 2020, *ApJ*, 890, 175
 Fouvy, J.-B., & Bar-Or, B. 2018, *MNRAS*, 481, 4566
 Gondolo, P., & Silk, J. 1999, *PhRvL*, 83, 1719
 Graham, A. W., & Spitler, L. R. 2009, *MNRAS*, 397, 2148
 Gürkan, M. A., & Hopman, C. 2007, *MNRAS*, 379, 1083
 Hamers, A. S., Portegies Zwart, S. F., & Merritt, D. 2014, *MNRAS*, 443, 355
 Levin, Y., Pakter, R., & Rizzato, F. B. 2008, *PhRvE*, 78, 021130
 Madigan, A.-M., Hopman, C., & Levin, Y. 2011, *ApJ*, 738, 99
 Madigan, A.-M., & Levin, Y. 2012, *ApJ*, 754, 42
 Merritt, D., Alexander, T., Mikkola, S., & Will, C. M. 2011, *PhRvD*, 84, 044024
 Nayakshin, S., Sazonov, S., & Sunyaev, R. 2012, *MNRAS*, 419, 1238
 Onsager, L. 1949, *NCim*, 6, 279
 Rauch, K. P., & Tremaine, S. 1996, *NewA*, 1, 149
 Roupas, Z., Kocsis, B., & Tremaine, S. 2017, *ApJ*, 842, 90
 Seth, A., Agüeros, M., Lee, D., & Basu-Zych, A. 2008, *ApJ*, 678, 116
 Sridhar, S., & Touma, J. R. 2016a, *MNRAS*, 458, 4129
 Sridhar, S., & Touma, J. R. 2016b, *MNRAS*, 458, 4143
 Szölglyén, A., & Kocsis, B. 2018, *PhRvL*, 121, 101101
 Touma, J., & Tremaine, S. 2014, *JPhA*, 47, 292001
 Touma, J., Tremaine, S., & Kazandjian, M. 2019, *PhRvL*, 123, 021103
 Tremaine, S. 1995, *AJ*, 110, 628
 Tremaine, S. 2005, *ApJ*, 625, 143
 Tremaine, S. 2020a, *MNRAS*, 491, 1941
 Tremaine, S. 2020b, *MNRAS*, 493, 2632